Crack geometry of serpentinized peridotites inferred from onboard ultrasonic data from the Oman Drilling Project

Ikuo Katayama, Natsue Abe, Keishi Okazaki, Kohei Hatakeyama, Yuya Akamatsu, Katsuyoshi Michibayashi, Marguerite Godard, Peter Kelemen

Tectonophysics 814 (2021) 228978

Contents lists available at ScienceDirect

Tectonophysics

journal homepage: www.elsevier.com/locate/tecto

Crack geometry of serpentinized peridotites inferred from onboard ultrasonic data from the Oman Drilling Project

Ikuo Katayama [a,*], Natsue Abe [b], Keishi Okazaki [c], Kohei Hatakeyama [a,1], Yuya Akamatsu [a], Katsuyoshi Michibayashi [d], Marguerite Godard [e], Peter Kelemen [f], The Oman Drilling Project Phase 2 Science Party

[a] Department of Earth and Planetary Systems Science, Hiroshima University, Hiroshima 739-8526, Japan
[b] Mantle Drilling Promotion Office, MarE3, JAMSTEC, Kanagawa 236-0001, Japan
[c] Kochi Institute for Core Sample Research, X-star, JAMSTEC, Kochi 783-8502, Japan
[d] Graduate School of Environmental Studies, Department of Earth and Planetary Sciences, Nagoya University, Aichi 464-8602, Japan
[e] Géosciences Montpellier, CNRS, Université de Montpellier, Montpellier 34095, France
[f] Lamont Doherty Earth Observatory, Columbia University, New York 10964, USA

ARTICLE INFO

Keywords:
Crack
Serpentinite
Oman Drilling Project
Elastic wave velocity
Mantle hydration

ABSTRACT

To assess the geometry of cracks in highly altered peridotites, we analyzed the ultrasonic velocity of serpentinized dunites and harzburgites collected by the Oman Drilling Project (Holes BA1B, 3A, and 4A). First, we estimated the hydrated fraction from grain density to obtain the porosity-free matrix velocity, which indicated complete serpentinization at shallow depths and decreasing hydration at greater depths. We assume that the difference between the solid matrix and measured onboard ultrasonic velocity is attributed to cracks with a spheroidal shape in the samples. Application of the effective medium theory to onboard data, such as P-wave velocity and porosity, indicates that the average pore aspect ratio is mostly between 0.1 and 0.01, and crack density varies from 0.58 to 0.02. We found a positive relationship between aspect ratio and hydrated fraction, suggesting a change in crack shape related to dissolution–precipitation processes during hydration. The relatively high aspect ratio and hence high fluid flux at shallow depths are also consistent with the onboard resistivity data and present-day hydration processes inferred from the borehole fluid chemistry. The inversion of ultrasonic data provides a series of elastic moduli that can be used to make a rough approximation of Poisson's ratio from the onboard data, which is a key physical property for interpreting geophysical observations in the oceanic lithosphere.

1. Introduction

Occurrences of serpentinite in the oceanic lithosphere, related to normal faults flanking slow spreading ridges, fracture zones, bending faults near subduction zones, and hydration of the “cold nose” of the mantle wedge, have been identified by recent geophysical observations (e.g., Reston et al., 2001; Bostock et al., 2002; Ranero et al., 2003; Grevemeyer et al., 2007; Escartín et al., 2008; Fujie et al., 2013; Naif et al., 2015). Although hydration reactions are probably promoted along the damaged zones (e.g., Hirose and Hayman, 2008), how aqueous fluids percolate into the mantle and the spatial extent of mantle serpentinization remain highly uncertain. In such a damaged zone, crack plays an important role as fluid pathways and largely influence the physical properties and hence seismic velocity.

Serpentinization of mantle rocks is accompanied by a volume increase, which may result in the development of cracks during hydration reactions (e.g., MacDonald and Fyfe, 1985). The formation of cracks increases permeability and reactive surfaces, and thus hydration reactions form a positive feedback system (e.g., O'Hanley, 1992; Boudier et al., 2005; Jamtveit et al., 2008; Kelemen and Hirth, 2012; Ulven et al., 2014; Shimizu and Okamoto, 2016; Zhu et al., 2016; Malvoisin et al., 2017; Evans et al., 2018). Serpentinization reactions also have an important role in the deep-sea biosphere, where reaction-generated CH_4, H_2, and possibly organic compounds support dense microbial

* Corresponding author.
E-mail address: katayama@hiroshima-u.ac.jp (I. Katayama).
[1] Now at Department of Education, Meisei University, Tokyo 191–8506, Japan.

https://doi.org/10.1016/j.tecto.2021.228978
Received 22 December 2020; Received in revised form 1 June 2021; Accepted 19 June 2021
Available online 25 June 2021

communities such as the Lost City hydrothermal vent fields (e.g., Früh-Green et al., 2003; Kelley et al., 2005).

The Oman Drilling Project sampled the Samail ophiolite sequences from the crust to mantle in nine diamond-cored and six rotary-drilled boreholes (Kelemen et al., 2013, 2020). The mantle sections are highly altered, and the borehole fluid chemistry indicates present-day hydration reactions are occurring (de Obeso et al., 2020). The recovered core samples were analyzed on the drilling vessel *Chikyu* during two 60-day description campaigns in 2017 and 2018. The continuous core samples are ideal for assessing serpentinization processes in mantle sequences, including crack development during hydration.

Elastic wave velocity of rocks depends on mineralogical composition, porosity, and pore fluid properties, but are also sensitive to pore structure. Effective medium theory has been widely applied to porous rocks, in which the change of elastic velocity is characterized by crack density and aspect ratio (e.g., Walsh, 1965; Kuster and Toksöz, 1974; O'Connell and Budiansky, 1977; Watanabe, 1993; Kachanov et al., 1994; Guéguen and Schubnel, 2003). Applications of such models to volcanic and gabbroic rocks collected by the Integrated Ocean Drilling Program (IODP) have succeeded in characterizing crack structures of core samples (e.g., Tsuji and Iturrino, 2008; Carlson, 2010). To assess the crack geometry in the highly altered peridotites collected by the Oman Drilling Project, we applied effective medium theory to onboard data measured during the description campaign. Our results yield the distribution and shapes of cracks in the drill core samples, which provide insights into mantle hydration processes.

2. Core samples and ultrasonic measurements

The Oman Drilling Project obtained continuous core samples from the dike–gabbro transition into the uppermost mantle in the Samail ophiolite (Kelemen et al., 2013, 2020). In this study, we focused on three boreholes of the mantle sections (BA1B, BA3A, and BA4A) that are each ~300–400 m in long (Fig. 1). The locations of the holes are given in Table 1. Core from Hole BA1B sampled an upper dunite section overlying a lower harzburgite section, both cut by abundant mafic dikes. Holes BA3A and BA4A consist dominantly of harzburgite and dunite, respectively, along with abundant mafic dikes. These mantle samples are highly altered, with >70% serpentinization, and only a few relicts of mantle olivine and orthopyroxene remain (Fig. 2). The dunite samples tend to be highly altered compared to the harzburgites. These highly altered peridotites have a mesh texture, which is typical of low-temperature serpentinite, and have a nearly random crystal fabric (e.g., Wicks and Whittaker, 1977).

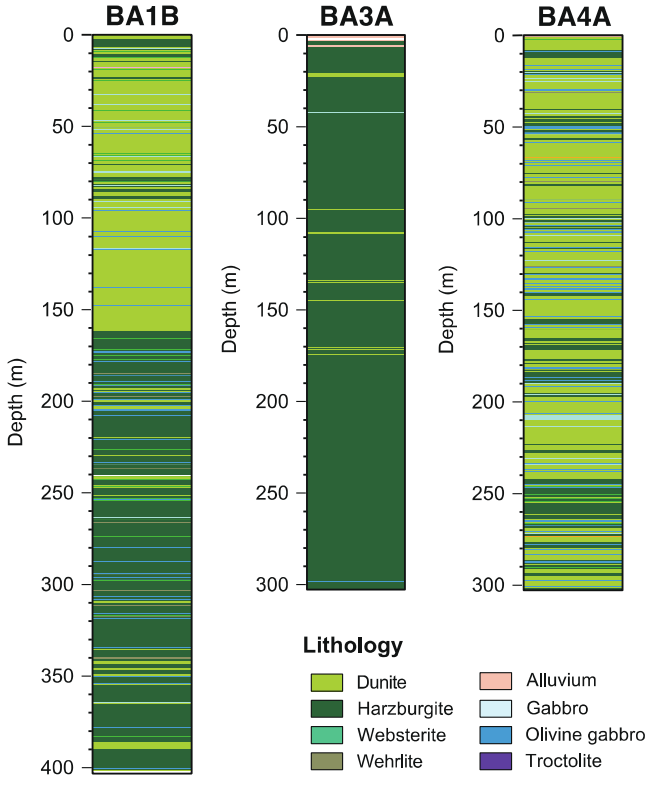

Fig. 1. Borehole stratigraphy of mantle sections from the Oman Drilling Project. Hole BA1B comprise the upper dunite section overlain the lower harzburgite section, and Holes BA3A and Hole 4A consist dominantly of harzburgite and dunite, respectively.

During core description campaigns on the drilling vessel *Chikyu,* the physical properties of the recovered core samples were systematically analyzed (Abe et al., 2018). The core samples were cut into ca. 2 × 2 × 2 cm cubes, and mass and volume were measured using the dual balance system and gas pycnometer. Grain density was calculated from the dry mass and solid volume, and porosity was calculated from the difference between dry and wet mass. We measured the P-wave velocity (V_P) in three orthogonal directions in core samples saturated with NaCl solution (3.5 g/L). The ultrasonic velocity measurements were carried out with a PWV-D system (GEOTEK) comprising P-wave transducers with a resonant frequency of 230 kHz, thickness and temperature sensors, and data processing software. The first arrival was identified by the system and the full waveform was stored on a computer. System calibration runs were conducted using a series of acrylic and glass cylinders of different thicknesses. We made eight measurements in each direction of the core samples, and used an average value, which typically results in <1% variation. Although the sample length is relatively short compared to the acoustic wavelength, the resonant frequency has a little influence on the measurement of ultrasonic velocity in these samples.

We measured three orthogonal directions, which showed a relatively weak anisotropy (<5%; Abe et al., 2018), and we therefore used the average velocity of the three orthogonal directions in this study. Although we measured core samples at ca. 3 m interval in each hole, including the mafic dikes, this study focused on the dunite and harzburgite samples in order to assess the crack geometry in the highly altered peridotites. The analyzed samples from each hole are listed in Table 1.

3. Ultrasonic data

Down-hole plots of P-wave velocity for each borehole are shown in Fig. 3 along with onboard measurements of grain density and porosity. The velocity of the dunite and harzburgite core samples ranges from 3.40 to 5.99 km/s, and tends to increase with increasing depth. The wide range of velocities reflects various amounts of hydration, and/or porosity. Since velocity and bulk density are both influenced by mineralogy and porosity, velocity shows a positive correlation with bulk density (Fig. 4a), but it is difficult to distinguish these effects. During

Table 1
Borehole locations and sample information.

Hole No.	Location	Latitude	Longitude	Total length	Analyzed samples
BA1B	Wadi Lawayni, Northern Sharqiyah	22°52.874′ N	58°42.035′ E	423.6 m	52 dunite, 75 harzburgite
BA3A	Wadi Lawayni, Northern Sharqiyah	22°51.970′ N	58°42.634′ E	314.4 m	2 dunite, 96 harzburgite
BA4A	Wadi Lawayni, Northern Sharqiyah	22°53.101′ N	58°41.703 E	323.9 m	66 dunite, 28 harzburgite

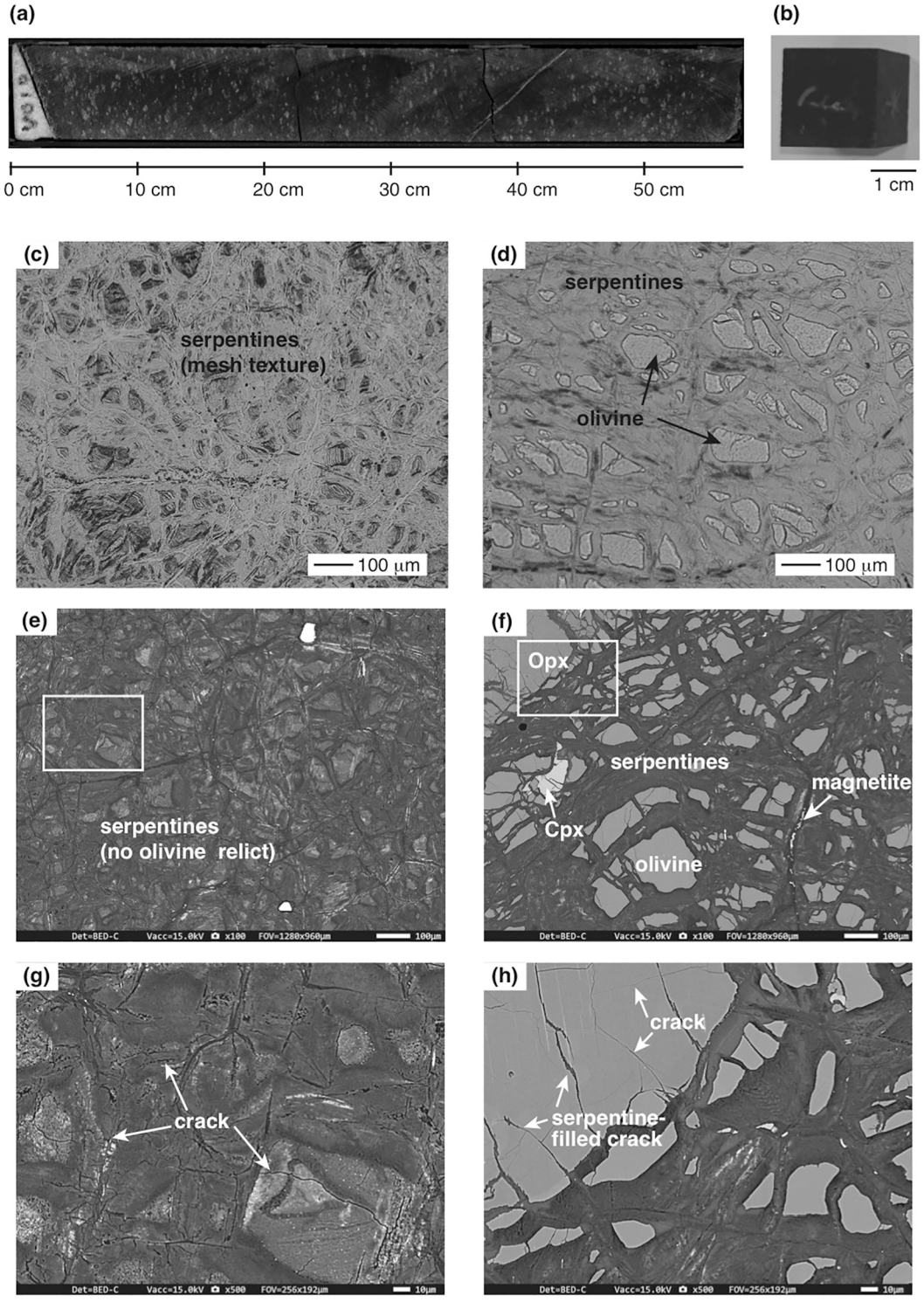

Fig. 2. (a) Recovered core sections of BA1B-123Z4. (b) Photographs of the cube samples. (c, d) Microphotographs of the dunite sample (BA1B-40Z-4) and the harzburgite (BA1B-134Z-4). (e, f) Backscattered electron images of the dunite and harzburgite samples. Olivine relicts can be seen in the harzburgite sample, while the dunite is mostly serpentinized. (g, h) Enlarged view of the back-scattered electron images showing cracks in these samples.

mantle hydration, P-wave velocity is known to decrease due to the hydration products such as serpentine and brucite (e.g., Christensen, 2004; Watanabe et al., 2007; Reynard, 2013). In addition, given the large contrast in elastic properties of solid and fluid, the presence of fluid-filled voids and/or cracks has a strong influence on ultrasonic velocity (e.g., Mavko et al., 2009). Fig. 5 shows the relationship between P-wave velocity and porosity, in which velocity decreases systematically with increasing porosity. To distinguish between the effects of hydration and porosity, we plotted the P-wave velocity as a function of grain density, which is sensitive to hydration products but insensitive to porosity (Fig. 4b). Serpentinite is characterized by a low velocity and low grain density compared to unaltered peridotite, resulting in a lower left trend due to hydration, while the effect of porosity results in a vertical trend that is independent of grain density. Fig. 4b shows that most onboard

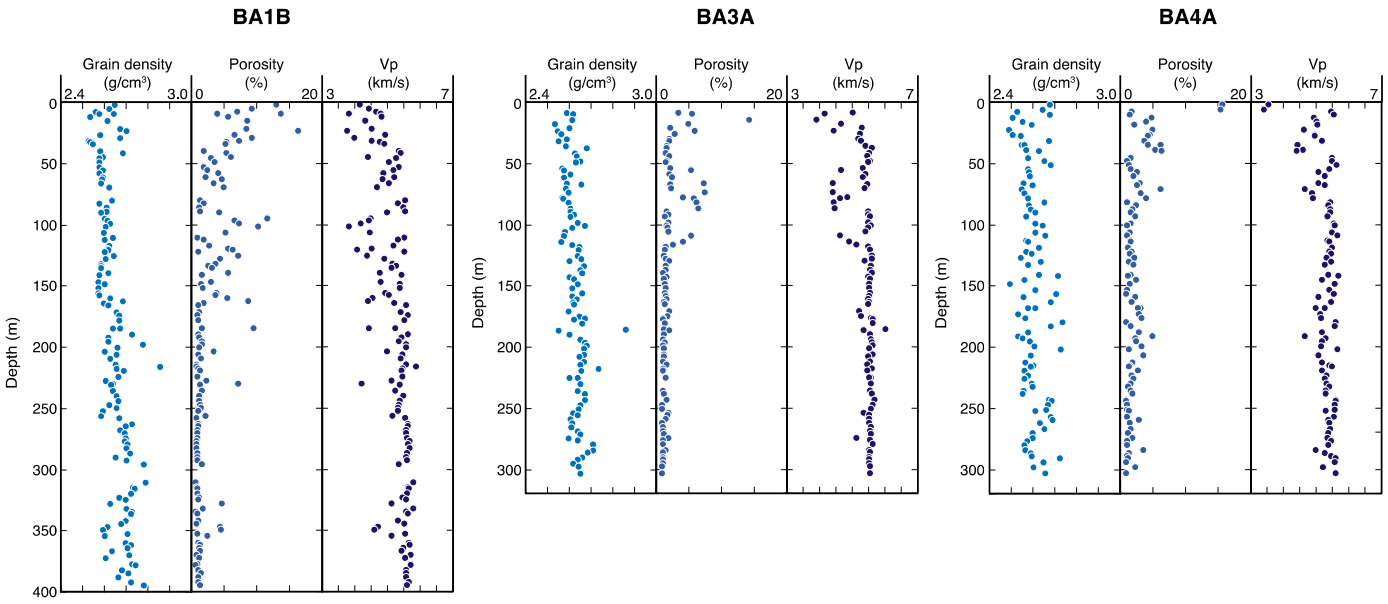

Fig. 3. Down-hole plots of grain density, porosity and P-wave velocity of the altered peridotites in the three boreholes (BA1B, BA3A, and BA4A). These physical properties were measured on the drilling vessel *Chikyu* during the description campaigns.

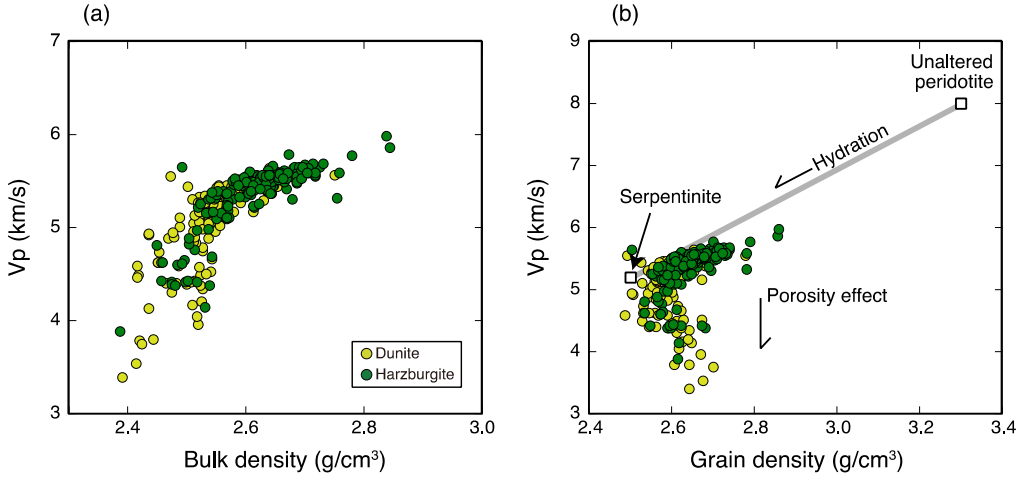

Fig. 4. (a) Relationship between P-wave velocity and bulk density. (b) Relationship between P-wave velocity and grain density. The gray line indicates the hydration trend from unaltered peridotite (V_P = 8.0 km/s; ρ_{grain} = 3.3 g/cm^3) to serpentinite (V_P = 5.2 km/s; ρ_{grain} = 2.5 g/cm^3).

data plot close to end-member serpentinite, indicating a high degree of alteration, but below the trend that reflects variable porosity.

4. Hydrated fraction

To assess the effect of crack geometry, we first estimated the influence of hydration (i.e., serpentinization). The hydrated fraction was calculated from grain density ρ_{grain} using the following linear relationship:

$$\rho_{grain} = A\rho_{serp} + (1-A)\rho_{perid} \quad (1)$$

where A is the hydrated fraction, and ρ_{serp} and ρ_{perid} are the porosity-free densities of serpentinite and unaltered peridotite, respectively (e.g., Christensen, 2004). We calculated the hydrated fraction using the reference density listed in Table 2. Because of variable chemical compositions even in the same mantle sequence, the reference values can vary due to modal abundance of constituent minerals, such as serpentine, brucite and magnetite. For instance, brucite has a slightly lower grain density than serpentine, and hence hydrated fraction can be overestimated for the sample with a relatively higher abundance of brucite. In contrast, magnetite has a higher grain density, which have the opposite effect. These variations of mineral proportions introduce the uncertainty of hydrated fraction, mostly ±10%. A few samples have a grain density lower than the end-member serpentinite, possibly due to a lower abundance of magnetite. We consider these as completely hydrated samples.

Fig. 6 shows profiles of the hydrated fraction in each borehole. Core samples are completely hydrated close to the surface, although the hydrated fraction tends to decrease with depth in Hole BA1B, down to ~70%. A similar hydration trend in these mantle sequences has been obtained from onboard analyses of loss of ignition (LOI) and X-ray CT imaging of the continuous core samples (Michibayashi et al., 2018; Kelemen et al., 2020). The increasing reaction progress upward is consistent with the borehole fluid chemistry, such as pH and oxygen fugacity (de Obeso et al., 2020), suggesting present-day hydration reactions are occurring during "top-down" weathering of the mantle sequences at these sites.

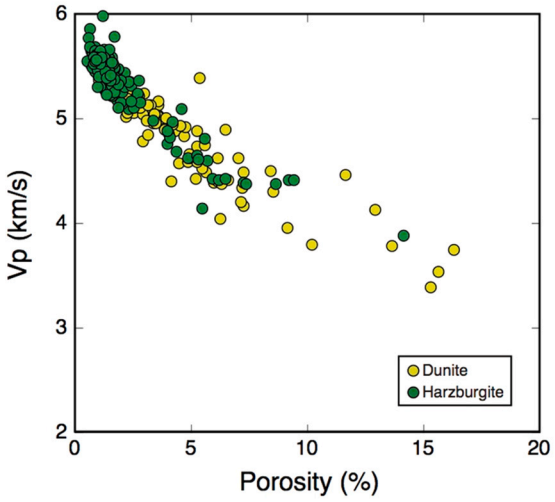

Fig. 5. Relationship between P-wave velocity and porosity.

Table 2
Seismic velocity and physical properties used in the crack model.

Unaltered peridotite	P-wave velocity (V_P)	8.0 km/s
	S-wave velocity (V_S)	4.5 km/s
	Poisson's ratio (σ)	0.27
	Density (ρ)	3.3 g/cm^3
	Bulk modulus (K)	122 GPa
	Shear modulus (G)	67 GPa
Serpentinite	P-wave velocity (V_P)	5.2 km/s
	S-wave velocity (V_S)	2.6 km/s
	Poisson's ratio (σ)	0.33
	Density (ρ)	2.5 g/cm^3
	Bulk modulus (K)	45 GPa
	Shear modulus (G)	17 GPa
Fluid	P-wave velocity (V_P)	1.5 km/s
	S-wave velocity (V_S)	–
	Poisson's ratio (σ)	0.5
	Density (ρ)	1.0 g/cm^3
	Bulk modulus (K)	2.2 GPa
	Shear modulus (G)	–

5. Calculation of crack aspect ratio and density

From the hydrated fraction, we calculated the P-wave velocity of the solid matrix ($V_{P,solid}$) for each core sample assuming a linear relationship between serpentinite and unaltered peridotite (Christensen, 2004) as follows:

$$V_{P,\ solid} = AV_{P,\ serp} + (1-A)V_{P,\ perid} \tag{2}$$

where $V_{P,serp}$ and $V_{P,perid}$ are the porosity-free P-wave velocities of serpentinite and peridotite, and A is the hydrated fraction inferred from the grain density. The difference between the calculated porosity-free matrix velocity and the measured onboard velocity is attributed to porosity and pore geometry. Numbers of theoretical models have been proposed to determine the effective elastic velocity of a material containing voids and/or cracks (e.g., Walsh, 1965; Kuster and Toksöz, 1974; O'Connell and Budiansky, 1974, 1977; Watanabe, 1993; Kachanov et al., 1994; Guéguen and Schubnel, 2003). All these models suggest that the elastic properties of such materials depend on porosity and pore fluid properties, but are also dependent on pore structures, such as the pore aspect ratio. In this study, we applied the classical model of Kuster and Toksöz (1974), because it is applicable over a wide range of aspect ratios, whereas most of other models, including the self-consistent theory of O'Connell and Budiansky (1977), are limited to small aspect ratios. Although the crack geometry and its interaction are different among these theoretical models, the porosity and velocity relationship is highly sensitive to the crack aspect ratio in any models (Fig. S1).

According to the long-wavelength first-order scattering theory of Kuster and Toksöz (1974), a pore is assumed to be a randomly oriented spheroidal inclusion that is characterized by aspect ratio, which is defined as the ratio of the polar to equatorial lengths. The distribution of pores with variable aspect ratios has been inferred by inversion of experimental data during hydrostatic loading to high pressure (Cheng and Toksöz, 1979). However, in this study we estimated an average aspect ratio for each core sample, because the measured onboard velocity data were only acquired at atmospheric pressure. For a two-phase material with solid matrix and pore fluid moduli, the effective bulk modulus K^* and shear modulus μ^* are dependent on porosity ϕ and aspect ratio α, as follows:

$$(K^* - K_s)\frac{K_s + 4/3\mu_s}{K^* + 4/3\mu_s} = \phi(K_f - K_s)\frac{K_s}{K_f + \pi\alpha\beta_S} \tag{3}$$

and

$$(\mu^* - \mu_s)\frac{\mu_s + \zeta_s}{\mu^* + \zeta_s} = \frac{-\mu_s\phi}{5}\left(1 + \frac{8\mu_s}{\pi\alpha(\mu_S + 2\beta_S)} + 2\frac{K_f + 2/3\mu_S}{K_f + \pi\alpha\beta_S}\right) \tag{4}$$

where the subscripts s and f refer to the solid matrix and fluid moduli, respectively. The coefficients β and ζ are expressed as

$$\beta = \mu\frac{3K + \mu}{3K + 4\mu} \tag{5}$$

and

$$\zeta = \frac{\mu(9K + 8\mu)}{6(K + 2\mu)} \tag{6}$$

These relationships were derived by Kuster and Toksöz (1974) and Berryman (1995). The assumptions involved in this derivation are sample homogeneity and an isotropic pore distribution in the solid matrix.

The results of the model calculation are shown in Fig. 7, with the measured onboard velocity normalized to the matrix velocity as a function of porosity. The relationship between the normalized velocity and porosity is dependent on the aspect ratio of the pores. Velocity is relatively insensitive to porosity for large aspect ratios (nearly spherical pores), but shows a marked decrease with increasing porosity for pores with a small aspect ratio. Most of the measured onboard data lies between the $\alpha = 0.1$ and 0.01 curves, which correspond to the average pore shape. We estimated the aspect ratio for each core sample using the measured velocity normalized to the porosity-free velocity calculated from the hydrated fraction, and the porosity determined by the moisture and density (MAD) analysis.

The pore aspect ratio is constrained for samples with a large difference between the solid matrix and measured onboard velocity, whereas the calculation has a large uncertainty when these velocities are nearly the same. As such, we did not analyze samples with a velocity difference less than 1.5%; this applied to only a few samples in each borehole. In the calculation of the pore structure, we assumed a spheroidal shape with an average aspect ratio, although pore shapes in the serpentinized peridotites are highly variable (Fig. 2), which results in a large uncertainty on the estimated pore aspect ratio. Equant pores can make a large contribution to porosity but have a weak effect on velocity, whereas thin cracks with small aspect ratios make a minor contribution to porosity but have a marked effect on velocity. Such bimodal pore distributions can be suitable for volcanic rocks (e.g., Adelinet et al., 2010). However, microcracking related to volume expansion appears to be the dominant mechanism for pore development in mantle rocks, and thus we used a single pore structure to simplify the calculations. Another source of uncertainty is the porosity-free matrix velocity used for calculations. Brucite has a slightly higher velocity than serpentine, as well as

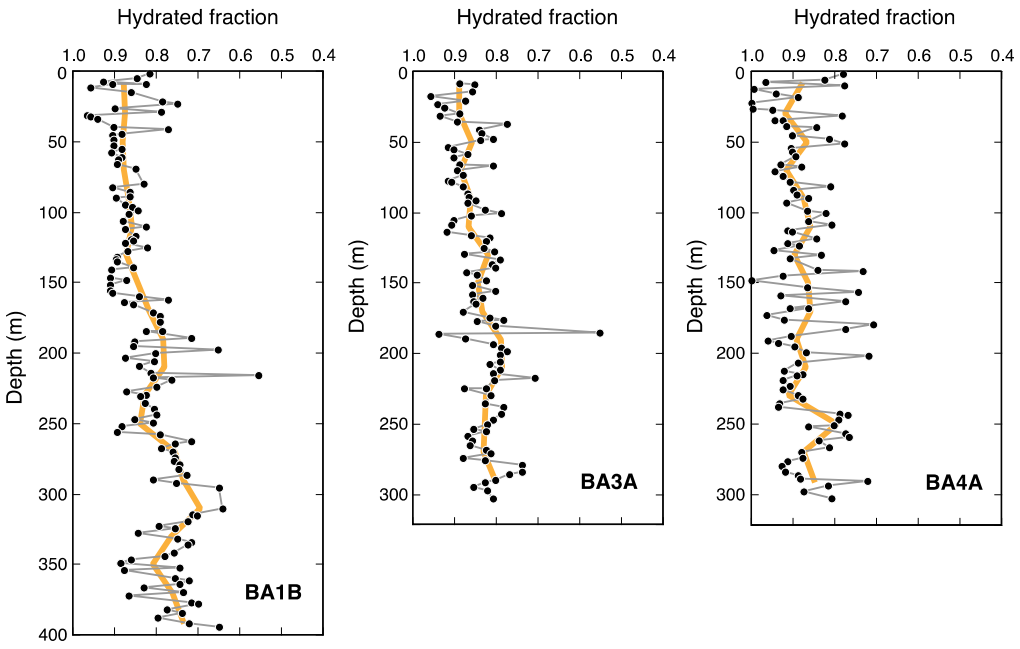

Fig. 6. Profiles of the hydrated fraction (serpentinization) inferred from grain density in the three boreholes. Orange lines are 20 m averaged profiles.

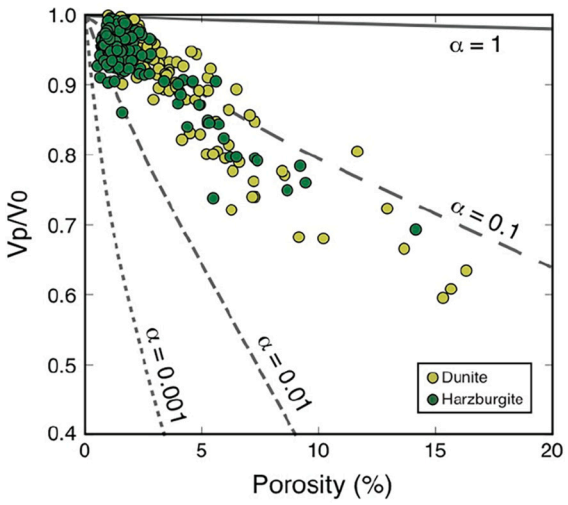

Fig. 7. Plot of P-wave velocity normalized to the porosity-free velocity versus porosity. Theoretical curves with different aspect ratios (α = 1, 0.1, 0.01, and 0.001) are shown, calculated from the effective medium theory of Kuster and Toksöz (1974).

orthopyroxene has a lower velocity than olivine for the end-member unaltered peridotite, and therefore the reference matrix velocities are influenced by the proportion of these minerals in addition to hydrated fraction. This leads a large uncertainty for samples with a small difference between the matrix and measured velocity, but the estimates of crack ratio are not much affected for samples showing a large difference. The specific porosity of chrysotile nanotubes has a potentially important consequence for modeling porosity effect on velocity; however, this effect is not incorporated in our calculations because water is unlikely infiltrated into the nanopores during the onboard analyses.

Down-hole plots of the calculated aspect ratio for pores in each borehole are shown in Fig. 8. The modeled aspect ratios mostly vary between 0.1 and 0.01, and show a slight decrease in aspect ratio with depth. This range of aspect ratios is broadly consistent with the pore shapes estimated for basalt and diabase collected during ocean drilling projects (Tsuji and Iturrino, 2008; Carlson, 2010). Assuming a spheroidal shape, and inferring from the data that most of the porosity corresponds to cracks, the porosity is related to crack density by $\phi = (4/3)\pi\alpha\varepsilon$, where ε is the crack density, which is the number of cracks per unit volume multiplied by the cube of the crack radius (e.g., Mavko et al., 2009). Given the calculated aspect ratio and porosity, and the influence that most of the porosity is in cracks, we calculated crack density profiles for each borehole (Fig. 9). Although the crack density is highest at shallow depths, it becomes small and nearly constant below about 100 m depth in all three holes. The crack density is locally high, even at deeper levels, which is possibly due to fault-damaged zones as that the structural descriptions of the same sections identified locally abundant macroscopic fractures and high vein densities (Kelemen et al., 2020).

6. Changes in crack geometry during hydration

The calculated crack aspect ratio has a positive correlation with the hydrated fraction, whereby the aspect ratio tends to increase with increasing degree of hydration (Fig. 10). The cracks in the altered peridotites were likely developed during hydration reactions due to the volume increase, and thus the change in the aspect ratio is potentially related to fluid flow and chemical exchange. Although pore shapes are highly variable in the samples, the dunites have relatively large crack apertures compared with those in the harzburgites (Fig. 2), consistent with the relatively large aspect ratios for the dunites inferred from the ultrasonic velocity data. Reaction-driven cracking is known to cause a positive feedback where new reactive surfaces are exposed and fluid pathways are created (e.g., O'Hanley, 1992; Jamtveit et al., 2008; Kelemen and Hirth, 2012; Ulven et al., 2014; Shimizu and Okamoto, 2016; Zhu et al., 2016; Malvoisin et al., 2017; Evans et al., 2018). Hydrothermal percolation experiments on olivine aggregates have shown that porosity of the reaction products varies little during fluid injection compared with the permeability change, suggesting a suite of coupled dissolution–precipitation reactions that are controlled at the pore scale by surface kinetic processes (Godard et al., 2013; Escario et al., 2018). In natural systems, the reaction process may vary depending on local fluid flux, but microstructural evidences of a coupled dissolution–precipitation mechanism are frequently observed in the serpentinized peridotites associated with fracturing (e.g., Plümper et al.,

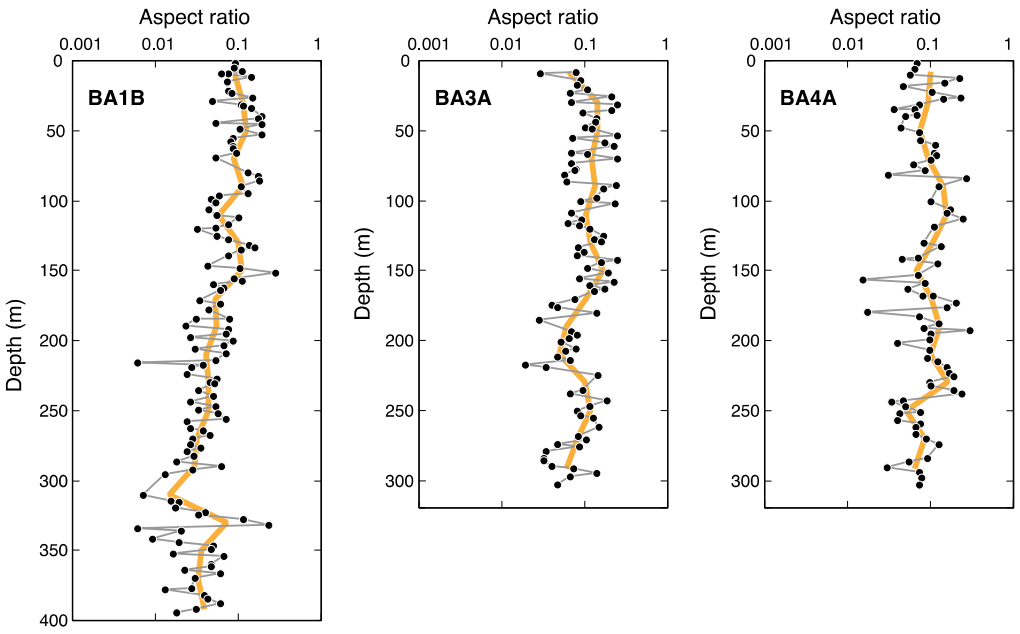

Fig. 8. Profiles of the calculated average aspect ratio of the altered peridotites in the three boreholes. Orange lines are 20 m averaged profiles.

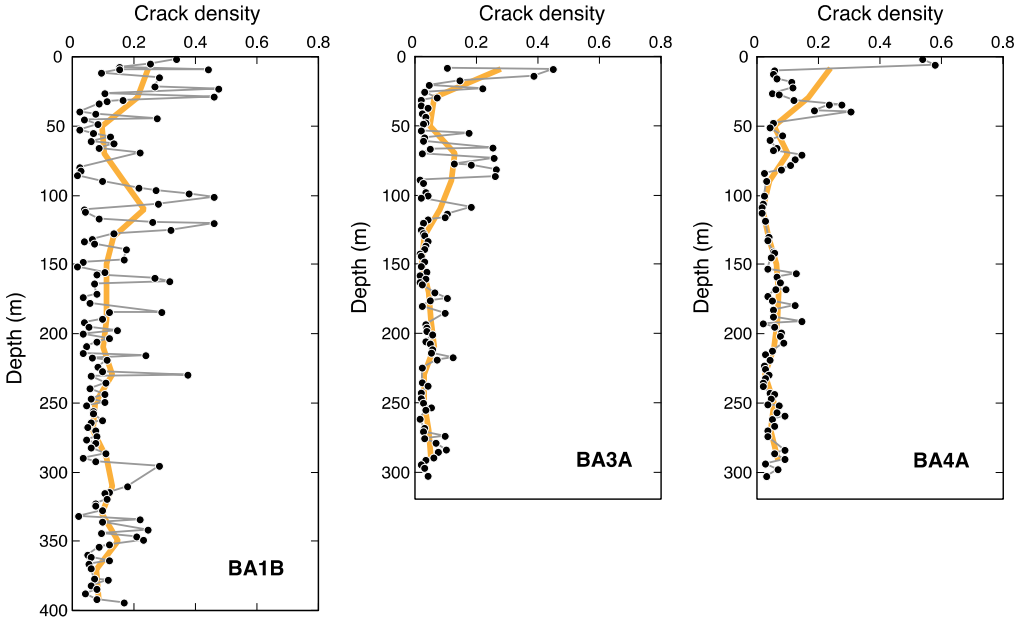

Fig. 9. Profiles of the calculated crack density of the altered peridotites in the three boreholes. Orange lines are 20 m averaged profiles.

2012).

The fluid flux due to laminar flow is mainly dependent on the conduit radius, and therefore the flow rate varies within cracks where a high fluid flux is expected in the widest part of a crack. This may result in a dissolution gradient in a fluid-percolated crack, and might cause a change in aspect ratio during reaction progress. High fluid flow may enhance dissolution, leading to a large aspect ratio at a high water/rock ratio. Wider cracks could also support higher precipitation rates. However, such cracks are also better connected and may maintain the permeable network in a positive feedback system. Different fluid transport rate may also change the reaction paths during serpentinization, where high fluid flux favors the development of Si-rich passivation layer at the reaction interface that maintains a permeable network and fluid penetration (Escario et al., 2018). Fluid chemistry and the upward increase in the hydrated fraction indicate present-day hydration is occurring in the boreholes sampled by the Oman Drilling Project (e.g., Kelemen et al., 2020), which is consistent with the crack distribution profile in these boreholes.

The onboard resistivity data also support “top-down” hydration processes, as the upper dunite sequence has a lower resistivity than the underlying harzburgite sequence, meaning that highly connected pore networks and reaction products occur at shallow depths. Application of the Hashin-Shtrikman bound to the resistivity data indicates a large transport porosity and, therefore, higher permeability at shallow levels (Katayama et al., 2020). As such, the relatively large crack aspect ratio is most likely associated with a high fluid flux. In the greater depths, some cracks might close as elevated confining pressure. According to the Walsh's model, thin crack can easily close under a relatively low pressure, whereas crack with large aspect ratio can survive at higher pressure (Walsh, 1965). The crack aspect ratio calculated from our analysis

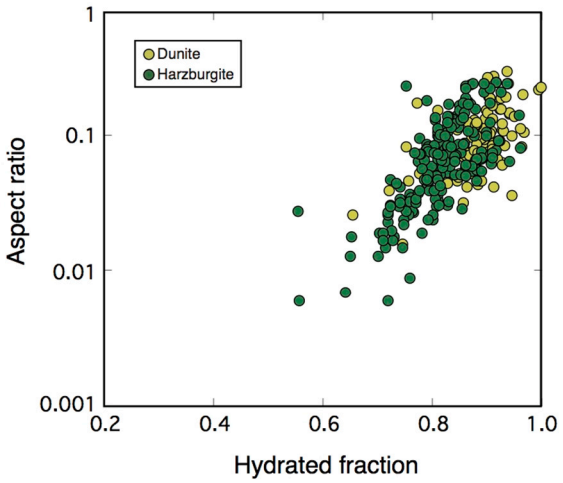

Fig. 10. Relationship between the crack aspect ratio and hydrated fraction.

is ranging from 0.01 to 0.1, which results in the closure pressures of 400–4000 MPa. This suggests that most cracks can remain open at the boreholes depths at pressure of ~10 MPa. Laboratory measurements of dredged serpentinites under confining pressure also indicate that most pores filled by aqueous fluid can survive at pressure as high as 200 MPa (Hatakeyama and Katayama, 2020).

7. Modeling of elastic moduli and geophysical implications

Seismic velocity is influenced by various factors, including mineralogy, porosity, and temperature, while Poisson's ratio in terms of V_P/V_S is considered a primary parameter controlled by mineralogy (e.g., Christensen, 1996). Serpentine minerals exhibit a markedly high Poisson's ratio ($\sigma = 0.33$). Hence, geophysical detection of anomalously high Poisson's ratios is commonly interpreted to reflect the presence of serpentine in the mantle (e.g., Christensen, 2004; Reynard, 2013). Although we only measured the P-wave velocity of core samples during the description campaign, the application of effective medium theory, incorporating porosity data, provides a full set of elastic constants such as the bulk and shear moduli. Fig. 11 shows the modeled results of the elastic moduli in Hole BA1B. Even though the simplified representation of crack properties, these calculated moduli makes possible to estimate S-wave velocity and Poisson's ratio of the core samples. In ocean drilling projects, the S-wave velocity of recovered samples was not always measured; however, this inversion approach can make rough approximations of S-wave velocity and Poisson's ratio from the existing P-wave velocity and porosity data.

The calculated Poisson's ratio for core samples from Hole BA1B is nearly constant, while the hydrated fraction tends to decrease with depth. This might be due to the influence of fluid-filled cracks, since effective medium theory predicts that Poisson's ratio is dependent on porosity and pore shape, as well as mineralogy. Increasing numbers of cracks with a small aspect ratio ($\alpha \sim 0.01$) in the altered peridotite results in a higher Poisson's ratio (given the same solid matrix), whereas cracks with a relatively large aspect ratio ($\alpha \sim 0.1$) have the opposite effect. In Hole BA1B, the hydrated fraction tends to decrease with depth, but the inferred aspect ratio also changes with depth. Consequently, these effects cancel each other, and the Poisson's ratio is nearly constant throughout this borehole.

Although we assumed a spheroidal pore shape, pore structures are variable in natural systems, and a pore tube model can be appropriate for high-pressure rocks and a partially molten rock. Takei (2002) developed an equilibrium geometry model, in which Poisson's ratio is characterized by a liquid volume fraction and dihedral angle. Differential effective medium (DEM) calculations also indicate the influence of fluid-filled pore shapes on Poisson's ratio (Brantut and David, 2019), and anisotropy caused by crack alignment can change Poisson's ratio depending on the direction of propagation of seismic energy (Wang et al., 2012). As such, the influence of pore geometry needs to be considered when interpreting the anomalously high Poisson's ratio observed in the mantle.

Recent geophysical surveys have revealed extensive hydration of oceanic mantle close to subduction trenches, due to water infiltration along the bending faults at the outer-rise regions (e.g., Grevemeyer et al., 2007; Contreras-Reyes et al., 2008; Van Avendonk et al., 2011; Fujie et al., 2013; Shillington et al., 2015; Obana et al., 2019). The degree of hydration and water contents have been estimated from seismic velocities using experimental data for partially serpentinized peridotites (e.g., Carlson and Miller, 2003). However, hydration reactions in the mantle are accompanied by crack development, and thus fluid-filled

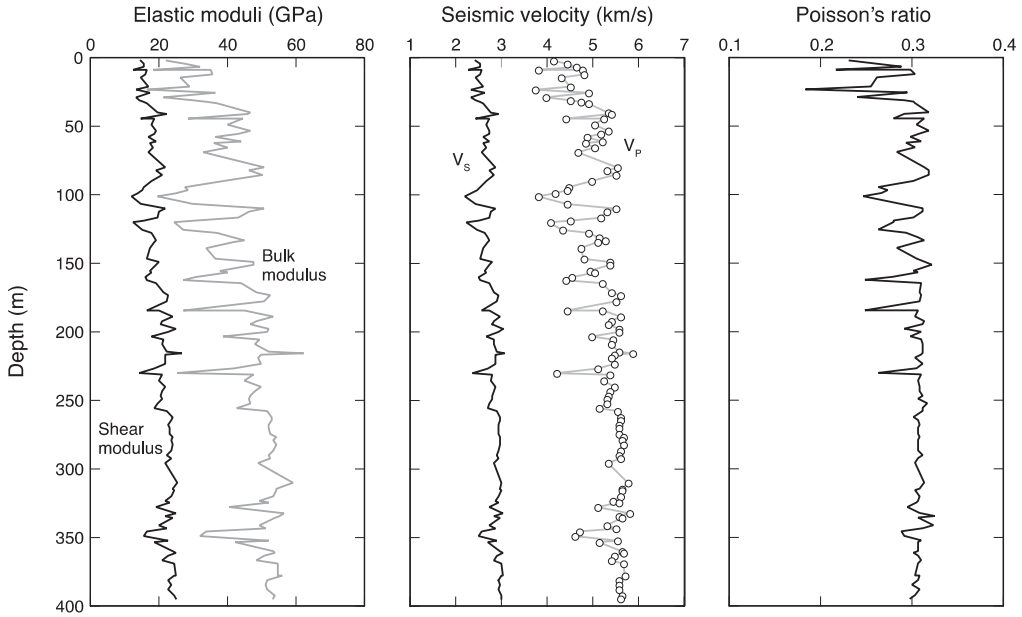

Fig. 11. Profiles of the calculated elastic moduli, seismic velocity and Poisson's ratio in Hole BA1B. Although the S-wave velocity was not measured, it was constrained from effective medium theory using the P-wave velocity and porosity.

porosity and pore shape are likely to affect the geophysical response. We therefore emphasize the importance of crack geometry for estimating the extent of serpentinization and water contents in the mantle. Recent experimental work by Hatakeyama and Katayama et al. (2020) obtained a relationship between seismic velocity and serpentinization, including the porosity effect, which suggests that previous estimates of serpentinization of outer-rise regions were overestimated because the proportion and aspect ratios of porosity were not considered. However, it is necessary to consider the frequency effect when applying these laboratory data to geophysical observations, because fluids stimulated by a high-frequency ultrasonic signal may undergo localized squirt flow, which affects the rock elastic properties in the laboratory. This effect is less significant for seismic data obtained at a low frequency (e.g., Dvorkin et al., 1995).

8. Conclusions

Application of effective medium theory to measured onboard data from the Oman Drilling Project, such as P-wave velocity and porosity, has revealed that the average crack aspect ratio in serpentinized peridotites varies from 0.1 to 0.01, and decreases slightly with depth in 300 to 400 m deep boreholes. A positive relationship between the aspect ratio and the hydrated fraction probably reflects a change in pore shape due to dissolution–precipitation reactions during hydration, which is consistent with the microstructural process of serpentinization associated with reaction-induced cracking. This inversion approach constrains the bulk and shear moduli, and hence Poisson's ratio was inferred from the P-wave velocity and porosity. Although our calculations are simplified and involve a number of assumptions, they can be applied to other borehole data, even if the S-wave velocity was determined during the onboard measurements of the core samples.

Supplementary data to this article can be found online at https://doi.org/10.1016/j.tecto.2021.228978.

Credit author statement

Ikuo Katayama: Conceptualization, Calculation, Writing, Natsue Abe, Keishi Okazaki, Kohei Hatakeyama, Yuya Akamatsu: Measurements, Reviewing, Katsuyoshi Michibayashi, Marguerite Godard, Peter Kelemen: Supervision, Reviewing and Editing.

Declaration of Competing Interest

The authors declare that they have no known competing financial interests or personal relationships that could have appeared to influence the work reported in this paper.

Acknowledgements

We thank Ulven, O. I., Hong, G., Zhu, W., and Cordonnier, B. for the measurements of physical properties during the description campaign at *Chikyu,* and Nagase, K. for preparing thin section of the samples. We also thank all members of the science party of the Oman Drilling Project. Comments from Guéguen, Y. and an anonymous reviewer greatly improved this manuscript. This research was supported by the Japan Society for the Promotion of Science (18H01321, 18H03733, and 20H00200).

References

Abe, N., et al., 2018. Initial report of physical property measurements, Chikyu Oman 2018: Crust-Mantle boundary and the mantle section from ICDP Oman Drilling Project Phase II. In: AGU Fall Meeting, V13E-0150. Washington D.C. USA.

Adelinet, M., Fortin, J., Guéguen, Y., Schubnel, A., Geoffroy, L., 2010. Frequency and fluid effects on elastic properties of basalt: experimental investigations. Geophys. Res. Lett. 37 https://doi.org/10.1029/2009GL041660.

Berryman, J.G., 1995. Mixture theories for rock properties. In: Ahrens, T.J. (Ed.), Rock Physics and Phase Relations, A Handbook of Physical Constants. AGU, Washington, D.C, pp. 205–228.

Bostock, M., Hyndman, R., Rondenay, S., Peacock, S., 2002. An inverted continental Moho and serpentinization of the forearc mantle. Nature 417, 536–538. https://doi.org/10.1038/417536a.

Boudier, F., Nicolas, A., Mainprice, D., 2005. Does anisotropy of thermal contraction control hydrothermal circulation at the moho level below fast spreading oceanic ridges? Int. Geol. Rev. 47, 101–112. https://doi.org/10.2747/0020-6814.47.1.101.

Brantut, N., David, E.C., 2019. Influence of fluids on V_P/V_S ratio: increase or decrease? Geophys. J. Int. 216, 2037–2043. https://doi.org/10.1093/gji/ggy518.

Carlson, R.L., 2010. How crack porosity and shape control seismic velocities in the upper oceanic crust: modeling downhole logs from Holes 504B and 1256D. Geochem. Geophys. Geosyst. 11 https://doi.org/10.1029/2009GC002955. Q04007.

Carlson, R.L., Miller, D.J., 2003. Mantle wedge water contents estimated from seismic velocities in partially serpentinized peridotites. Geophys. Res. Lett. 30 https://doi.org/10.1029/2002GL016600.

Cheng, C.H., Toksöz, M.N., 1979. Inversion of seismic velocities for the pore aspect ratio spectrum of a rock. J. Geophys. Res. 84, 7533–7543. https://doi.org/10.1029/JB084iB13p07533.

Christensen, N.I., 1996. Poisson's ratio and crustal seismology. J. Geophys. Res. 101 (B2), 3139–3156. https://doi.org/10.1029/95JB03446.

Christensen, N.I., 2004. Serpentinites, peridotites, and seismology. Int. Geol. Rev. 46, 795–816. https://doi.org/10.2747/0020-6814.46.9.795.

Contreras-Reyes, E., Grevemeyer, I., Flueh, E.R., Reichert, C., 2008. Upper lithospheric structure of the subduction zone offshore of southern Arauco peninsula, Chile, at ~38°S. J. Geophys. Res. 113 https://doi.org/10.1029/2007JB005569. B07303.

de Obeso, C.C., Godard, M., Kelemen, P., Matter, J., 2020. Low temperature alteration of peridotite, Samail ophiolite, Oman. In: Field Trip Guide, International Conference on Ophiolites and the Oceanic Lithosphere: Results of the Oman Drilling Project and Related Research, pp. 1–40.

Dvorkin, J., Mavko, G., Nur, A., 1995. Squirt flow in fully saturated rocks. Geophysics 60, 97–107. https://doi.org/10.1190/1.1443767.

Escario, S., Godard, M., Gouze, P., Leprovost, R., 2018. Experimental study of the effects of solute transport on reaction paths during incipient serpentinization. Lithos 323, 191–207. https://doi.org/10.1016/j.lithos.2018.09.020.

Escartín, J., et al., 2008. Central role of detachment faults in accretion of slow-spreading oceanic lithosphere. Nature 455, 790–794. https://doi.org/10.1038/nature07333.

Evans, O., Spiegelman, M., Kelemen, P.B., 2018. A poroelastic model of serpentinization: exploring the interplay between rheology, surface energy, reaction, and fluid flow. J. Geophys. Res. 123, 8653–8675. https://doi.org/10.1029/2017JB015214.

Früh-Green, G.L., Kelley, D.S., Bernasconi, S.M., Karson, J.A., Ludwig, K.A., Butterfield, D.A., et al., 2003. 30,000 years of hydrothermal activity at the Lost City vent field. Science 301, 495–498. https://doi.org/10.1126/science.1085582.

Fujie, G., Kodaira, S., Yamashita, M., Sato, T., Takahashi, T., Takahashi, N., 2013. Systematic changes in the incoming plate structure at the Kuril trench. Geophys. Res. Lett. 40, 88–93. https://doi.org/10.1029/2012GL054340.

Godard, M., Luquot, L., Andreani, M., Gouze, P., 2013. Incipient hydration of mantle lithosphere at ridges: a reactive-percolation experiment. Earth Planet. Sci. Lett. 371, 92–102. https://doi.org/10.1016/j.epsl.2013.03.052.

Grevemeyer, I., Ranero, C.R., Flueh, E.R., Kläschen, D., Bialas, J., 2007. Passive and active seismological study of bending-related faulting and mantle serpentinization at the Middle America trench. Earth Planet. Sci. Lett. 258, 528–542. https://doi.org/10.1016/j.epsl.2007.04.013.

Guéguen, Y., Schubnel, A., 2003. Elastic wave velocities and permeability of cracked rocks. Tectonophysics 370, 163–176. https://doi.org/10.1016/S0040-1951(03)00184-7.

Hatakeyama, K., Katayama, I., 2020. Pore fluid effects on elastic wave velocities of serpentinite and implications for estimates of serpentinization in oceanic lithosphere. Tectonophysics 775. https://doi.org/10.1016/j.tecto.2019.228309.

Hirose, T., Hayman, N.W., 2008. Structure, permeability, and strength of a fault zone in the footwall of an oceanic core complex, the Central Dome of the Atlantis Massif, Mid-Atlantic Ridge, 30°N. J. Struct. Geol. 30, 1060–1071. https://doi.org/10.1016/j.jsg.2008.04.009.

Jamtveit, B., Malthe-Sørenssen, A., Kostenko, O., 2008. Reaction enhanced permeability during retrogressive metamorphism. Earth Planet. Sci. Lett. 267, 620–627. https://doi.org/10.1016/j.epsl.2007.12.016.

Kachanov, M., Tsukrov, I., Shafiro, B., 1994. Effective moduli of solids with cavities of various shapes. Appl. Mech. Rev. 47, 152–174. https://doi.org/10.1115/1.3122810.

Katayama, I., et al., 2020. Permeability profiles across the crust-mantle sections in the Oman Drilling Project inferred from dry and wet resistivity data. J. Geophys. Res. 125 https://doi.org/10.1029/2019JB018698.

Kelemen, P.B., Hirth, G., 2012. Reaction-driven cracking during retrograde metamorphism: olivine hydration and carbonation. Earth Planet. Sci. Lett. 345, 81–89. https://doi.org/10.1016/j.epsl.2012.06.018.

Kelemen, P., et al., 2013. Scientific drilling and related research in the Samail Ophiolite, Sultanate of Oman. Sci. Drill. 15, 64–71.

Kelemen, P.B., Matter, J.M., Teagle, D.A.H., Coggon, J.A., The Oman Drilling Project Science Team, 2020. Proceedings of the Oman Drilling Project. International Ocean Discovery Program, College Station, TX.

Kelley, D.S., Karson, J.A., Früh-Green, G.L., Yoerger, D.R., Shank, T.M., Butterfield, D.A., et al., 2005. A serpentinite-hosted ecosystem: the Lost City hydrothermal field. Science 307, 1428–1434. https://doi.org/10.1126/science.1102556.

Kuster, G.T., Toksöz, M.N., 1974. Velocity and attenuation of seismic waves in two-phase media: part I. Theoretical formulations. Geophysics 39, 587–606. https://doi.org/10.1190/1.1440450.

MacDonald, A.H., Fyfe, W.S., 1985. Rate of serpentinization in seafloor environments. Tectonophysics 116, 123–135. https://doi.org/10.1016/0040-1951(85)90225-2.

Malvoisin, B., Brantut, N., Kaczmarek, M.-A., 2017. Control of serpentinization rate by reaction-induced cracking. Earth Planet. Sci. Lett. 476, 143–152. https://doi.org/10.1016/j.epsl.2017.07.042.

Mavko, G., Mukerji, T., Dvorkin, J., 2009. The Rock Physics Handbook: Tools for Seismic Analysis of Porous Media, 524 pp. Cambridge Univ. Press, Cambridge, U.K.

Michibayashi, K., Katayama, I., Kelemen, P., Okazaki, K., Godard, M., Takazawa, E., Teagle, D., The Oman Drilling Project Phase II Science Party, 2018. Quantification of the downhole degree of serpentinization estimated by X-ray CT core imaging. In: AGU Fall Meeting, V12B-01. Washington D.C. USA.

Naif, S., Key, K., Constable, S., Evans, R.L., 2015. Water-rich bending faults at the Middle America Trench. Geochem. Geophys. Geosyst. 16, 2582–2597. https://doi.org/10.10002/2015GC005927.

Obana, K., Fujie, G., Takahashi, T., Yamamoto, Y., Tonegawa, T., Miura, S., Kodaira, S., 2019. Seismic velocity structure and its implications for oceanic mantle hydration in the trench-outer rise of the Japan Trench. Geophys. J. Int. 217, 1629–1642. https://doi.org/10.1093/gji/ggz099.

O'Connell, R.J., Budiansky, B., 1974. Seismic velocities in dry and saturated cracked solids. J. Geophys. Res. 79, 5412–5426. https://doi.org/10.1029/JB079i035p05412.

O'Connell, R.J., Budiansky, B., 1977. Viscoelastic properties of fluid- saturated cracked solids. J. Geophys. Res. 82, 5719–5735. https://doi.org/10.1029/JB082i036p05719.

O'Hanley, D.S., 1992. Solution to the volume problem in serpentinization. Geology 20, 705–708. https://doi.org/10.1130/0091-7613.

Plümper, O., Røyne, A., Magrasó, A., Jamtveit, B., 2012. The interface-scale mechanism of reaction-induced fracturing during serpentinization. Geology 40, 1103–1106. https://doi.org/10.1130/g33390.1.

Ranero, C.R., Morgan, J.P., McIntosh, K., Reichert, C., 2003. Bending-related faulting and mantle serpentinization at the Middle America trench. Nature 425, 367–373. https://doi.org/10.1038/nature01961.

Reston, T.J., Pennell, J., Stubenrauch, A., Walker, I., Perez-Gussinye, M., 2001. Detachment faulting, mantle serpentinization, and serpentinite- mud volcanism beneath the Porcupine Basin, southwest of Ireland. Geology 29, 587–590. https://doi.org/10.1130/0091-7613.

Reynard, B., 2013. Serpentine in active subduction zones. Lithos 178, 171–185. https://doi.org/10.1016/j.lithos.2012.10.012.

Shillington, D.J., Becel, A., Nedimovic, M.R., Kuehn, H., Webb, S.C., Abers, G.A., Keranen, K.M., Li, J., Delescluse, M., Mattei-Salicrup, G.A., 2015. Link between plate fabric, hydration and subduction zone seismicity in Alaska. Nat. Geosci. 8, 961–964. https://doi.org/10.1038/ngeo2586.

Shimizu, H., Okamoto, A., 2016. The roles of fluid transport and surface reaction in reaction-induced fracturing, with implications for the development of mesh textures in serpentinites. Contrib. Mineral. Petrol. 171 https://doi.org/10.1007/s00410-016-1288-y.

Takei, Y., 2002. Effect of pore geometry on V_P/V_S: from equilibrium geometry to crack. J. Geophys. Res. 107, 2043 https://doi.org/10.1029/2001JB000522.

Tsuji, T., Iturrino, G.J., 2008. Velocity-porosity relationships in oceanic basalt from eastern flank of the Juan de Fuca Ridge: the effect of crack closure on seismic velocity. Explor. Geophys. 39, 41–51. https://doi.org/10.1071/EG08001.

Ulven, O.I., Jamtveit, B., Malthe-Sørenssen, A., 2014. Reaction-driven fracturing of porous rock. J. Geophys. Res. 119, 7473–7486. https://doi.org/10.1002/2014JB011102.

Van Avendonk, H.J.A., Holbrook, W.S., Lizarralde, D., Denyer, P., 2011. Structure and serpentinization of the subducting Cocos plate offshore Nicaragua and Costa Rica. Geochem. Geophys. Geosyst. 12 https://doi.org/10.1029/2011GC003592.

Walsh, J.B., 1965. The effect of cracks on the compressibility of rocks. J. Geophys. Res. 70, 381–389. https://doi.org/10.1029/JZ070i002p00381.

Wang, X.-Q., Schubnel, A., Fortin, J., David, E.C., Guéguen, Y., Ge, H.-K., 2012. High V_P/V_S ratio: saturated cracks of anisotropy effects? Geophys. Res. Lett. 39, L11307 https://doi.org/10.1029/2012GL051742.

Watanabe, T., 1993. Effects of water and melt on seismic velocities and their application to characterization of seismic reflectors. Geophys. Res. Lett. 20, 2933–2936. https://doi.org/10.1029/93GL03170.

Watanabe, T., Kasami, H., Ohshima, S., 2007. Compressional and shear wave velocities of serpentinized peridotites up to 200 MPa. Earth Planets Space 59, 233–244. https://doi.org/10.1186/BF03353100.

Wicks, F.J., Whittaker, E.J.W., 1977. Serpentine textures and serpentinization. Can. Mineral. 15, 459–488.

Zhu, W., Fusseis, F., Lisabeth, H., Xing, T., Xiao, X., De Andrade, V., Karato, S., 2016. Experimental evidence of reaction-induced fracturing during olivine carbonation. Geophys. Res. Lett. 18, 9535–9543. https://doi.org/10.1002/2016GL070834.